

PAPER

First ERO2.0 modeling of Be erosion and non-local transport in JET ITER-like wall





To cite this article: J Romazanov *et al* 2017 *Phys. Scr.* **2017** 014018

View the [article online](#) for updates and enhancements.

Related content

- [Material migration studies with an ITER first wall panel proxy on EAST](#)
R. Ding, R.A. Pitts, D. Borodin et al.
- [Study of physical and chemical assisted physical sputtering of beryllium in the JET ITER-like wall](#)
S. Brezinsek, M.F. Stamp, D. Nishijima et al.
- [Determination of Be sputtering yields from spectroscopic observations at the JET ITER-like wall based on three-dimensional ERO modelling](#)
D Borodin, S Brezinsek, J Miettunen et al.

First ERO2.0 modeling of Be erosion and non-local transport in JET ITER-like wall

J Romazanov¹ , D Borodin^{1,7} , A Kirschner¹ , S Brezinsek¹ ,
S Silburn², A Huber¹, V Huber³, H Bufferand³, M Firdaouss³ , D Brömmel⁴,
B Steinbusch⁴, P Gibbon⁴ , A Lasa⁵ , I Borodkina^{1,6}, A Eksaeva^{1,6},
Ch Linsmeier¹  and JET Contributors⁸

¹ Forschungszentrum Jülich GmbH, Institut für Energie- und Klimaforschung—Plasmaphysik, Partner of the Trilateral Euregio Cluster (TEC), D-52425 Jülich, Germany

² Culham Centre for Fusion Energy, Abingdon OX14 3DB, United Kingdom

³ CEA, IRFM, F-13108 St Paul-Lez-Durance, France

⁴ Forschungszentrum Jülich GmbH, Institute for Advanced Simulation, Jülich Supercomputing Centre, D-52425 Jülich, Germany

⁵ Oak Ridge National Laboratory, Oak Ridge, TN 37831-6169, United States of America

⁶ National Research Nuclear University MEPhI, 31, Kashirskoe sh., 115409, Moscow, Russia

E-mail: j.romazanov@fz-juelich.de

Received 28 May 2017, revised 28 August 2017

Accepted for publication 1 September 2017

Published 19 September 2017



CrossMark

Abstract

ERO is a Monte-Carlo code for modeling plasma-wall interaction and 3D plasma impurity transport for applications in fusion research. The code has undergone a significant upgrade (ERO2.0) which allows increasing the simulation volume in order to cover the entire plasma edge of a fusion device, allowing a more self-consistent treatment of impurity transport and comparison with a larger number and variety of experimental diagnostics. In this contribution, the physics-relevant technical innovations of the new code version are described and discussed. The new capabilities of the code are demonstrated by modeling of beryllium (Be) erosion of the main wall during JET limiter discharges. Results for erosion patterns along the limiter surfaces and global Be transport including incident particle distributions are presented. A novel synthetic diagnostic, which mimics experimental wide-angle 2D camera images, is presented and used for validating various aspects of the code, including erosion, magnetic shadowing, non-local impurity transport, and light emission simulation.

Keywords: beryllium, erosion, ERO, JET ITER-like wall

(Some figures may appear in colour only in the online journal)

1. Introduction

The fusion reactor ITER, which is currently under construction, will be equipped with a metallic first wall (FW), composed of beryllium (Be) in the main chamber and tungsten (W) in the divertor [1]. Erosion of Be reduces the lifetime of the main chamber plasma-facing components (PFCs) and increases impurity content in the plasma, which leads to

cooling and fuel dilution and thus decreases the performance of the fusion reactor. Furthermore, co-deposition with Be enhances the retention of fuel atoms in the FW, which should be minimized for safety and fuel cycle reasons. Hence, understanding Be erosion and migration is one of the key issues for ITER.

The Joint European Torus (JET), which is equipped with an ITER-like wall (ILW) [2], is an ideal test-bed for experimentally investigating this topic. A compilation of results achieved during the first years of operation with the ILW, along with a comparison with the former carbon wall (JET-C) and conclusions drawn for ITER, can be found in [3]. The

⁷ JARA-HPC, Jülich Supercomputing Centre, Forschungszentrum Jülich GmbH, Jülich D-52425, Germany.

⁸ See the author list of 'Overview of the JET results in support to ITER' by Litaudon *et al Nucl. Fusion* **57** 102001.

ILW also offers the opportunity of verifying modeling tools such as the Monte-Carlo code ERO [4], which was previously used for estimating the lifetime of ITER Be blanket modules [5]. Due to following eroded particles in 3D with full resolution of the gyromotion of ions, ERO can efficiently describe effects such as prompt deposition of heavy ions such as W [6–8], and also allows verification using experimental data e.g. from line-of-sight (LOS) integrated spectroscopy [7–10] or post-mortem analysis [7, 8, 11]. While ERO was designed for investigating simulation volumes of typically much smaller size than 1 m^3 , it is desirable to increase this size significantly in order to obtain a more complete and self-consistent model. This would also allow code verification using a larger number and variety of experimental diagnostics, which are usually situated at various locations.

For this purpose, the ERO code has undergone a significant upgrade. While the new version 2.0 relies on the same scientific assumptions as before (details on these can be found in [12]), the volume can now be increased to cover the entire plasma edge of a JET or ITER size fusion device in 3D. In order to demonstrate the new modeling capabilities enabled by the increased simulation volume, we present first ERO2.0 simulations for Be erosion in the main chamber during JET ILW limiter discharges. Modeling results for erosion patterns on the Be limiters, as well as for spatial Be impurity density distribution in the plasma and distributions of impact energy and angle of Be particles on PFCs, are discussed. Additionally, a novel synthetic diagnostic, which mimics experimental wide-angle 2D camera images, is presented. In addition to the LOS integrated spectroscopy previously used for validating ERO results, the 2D images offer the advantage of spatially resolved information and thus allow a more comprehensive validation.

2. ERO2.0 code

In this section, the relevant code improvements introduced by ERO2.0 will be illustrated. In the following text, the labels ‘ERO1.0’/‘ERO2.0’ will be used to refer to a specific code version and ‘ERO’ to refer to both versions.

The first improvement is a more flexible representation of the wall geometry in the code. ERO1.0 defines a local coordinate system (x, y, z) , with x and y being in-plane with an investigated wall part and z pointing radially away from it (see e.g. figure 1 in [5]). The wall is defined as a 2D matrix of (typically quadrilateral) computational surface cells for which plasma-wall interaction (PWI) processes are calculated and results are stored. The cells are regularly spaced in the (x, y) -plane, with the height $z(x, y)$ given at the center of each cell, thus defining the wall geometry. The use of these local coordinates is convenient for the simulation of selected PFC parts, but becomes increasingly inadequate for larger simulation volumes with complexly shaped wall components. ERO2.0 therefore allows using cylindrical coordinates (R, ϕ, z) , with $z = 0$ at the mid-plane of a toroidal fusion device, and treats the wall geometry as a polygon mesh in 3D, with each polygon representing a computational surface cell

(for practical reasons, only triangles and quadrilaterals are used). Figure 3 shows the polygon mesh used for the ERO2.0 simulations of the JET ILW in the present contribution, and is discussed in more detail below in section 3.2.

The second improvement is the massive parallelization of the code. The simulation of larger volumes with ERO increases the code execution time and memory demand. The execution time is determined by the computationally expensive calculation of particle trajectories, which increases with the volume size because 1) more computational particles (‘test particles’) are required to obtain sufficient statistics, and 2) each particle can travel much longer distances before it either re-deposits on a PFC or leaves the simulation volume boundaries. The memory demand is determined by the sizes of 3D grids on which plasma parameters and particle densities are stored, and therefore also increases with volume size if the grid resolution is kept constant.

Modern supercomputers such as JURECA [13] (which was used for the simulations in this work) are often distributed shared memory systems. They consist of many computational nodes, each of which is internally a shared memory system (i.e. it has its own local memory which is shared by the CPU cores of the node). ERO2.0 is massively parallelized and can be run on many nodes simultaneously using both distributed and shared memory parallelization in a hybrid approach. Thereby it benefits from the increased amount of both computational power (due to the many CPU cores) and memory of a supercomputer.

For the discussion of parallel performance, it is useful to distinguish between strong and weak scaling [14]. Strong scaling keeps the problem size fixed while increasing the number of CPU cores p in order to reduce the execution time $T(p)$. Weak scaling increases the problem size proportionally to p (the problem size per CPU core is fixed) in order to keep $T(p)$ constant for large problems. The aim of ERO2.0 is to increase the problem size, therefore we are mainly interested in weak scaling.

Figure 1 shows weak scaling measurements of ERO2.0 execution time on JURECA. Here, the particle number n is taken as a measure of the problem size. The number of CPU cores p is increased from 1 to 1536 (corresponding to 64 JURECA nodes with 24 CPU cores each). The particle number $n(p)$ is scaled accordingly, with $n(1) \approx 1300$. We observe a mild increase in execution time by a factor of $T(1500)/T(1) \approx 3$. This reflects the increasing fraction of time each core spends communicating with other cores. However, the increase of $T(p)$ by 3 is an acceptable cost for calculating $1500\times$ more test particles. Figure 1 also shows that the increase in $T(p)$ is roughly linear for the range of p examined here, therefore we can expect the parallelization to be efficient also for higher numbers of cores.

Additionally to the flexible wall geometry and massive parallelization, ERO2.0 introduces a number of other technical improvements:

- Optimization of time-consuming computational geometry operations, such as locating intersections between particle trajectories and wall elements (required for simulating

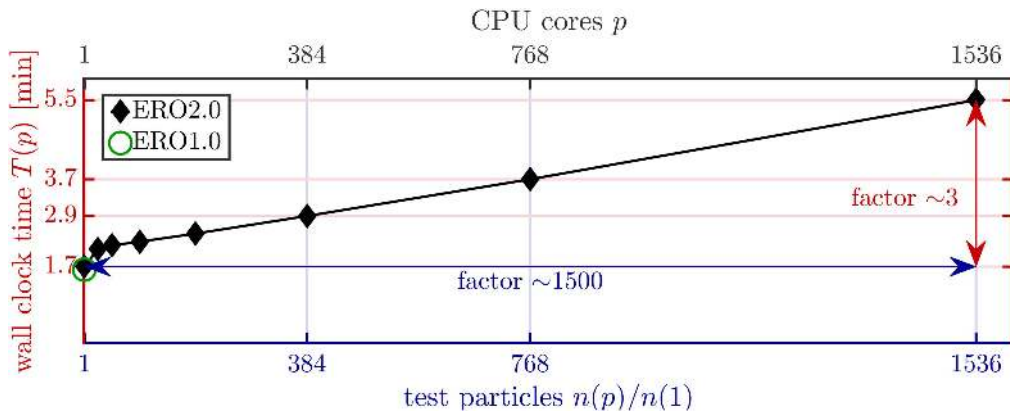


Figure 1. Parallel performance measurements using the Jülich supercomputer JURECA. The number of particles $n(p)$ is increased proportionally to the number of CPU cores p (weak scaling) with $n(1) \approx 1300$. The code execution time $T(p)$ is measured.

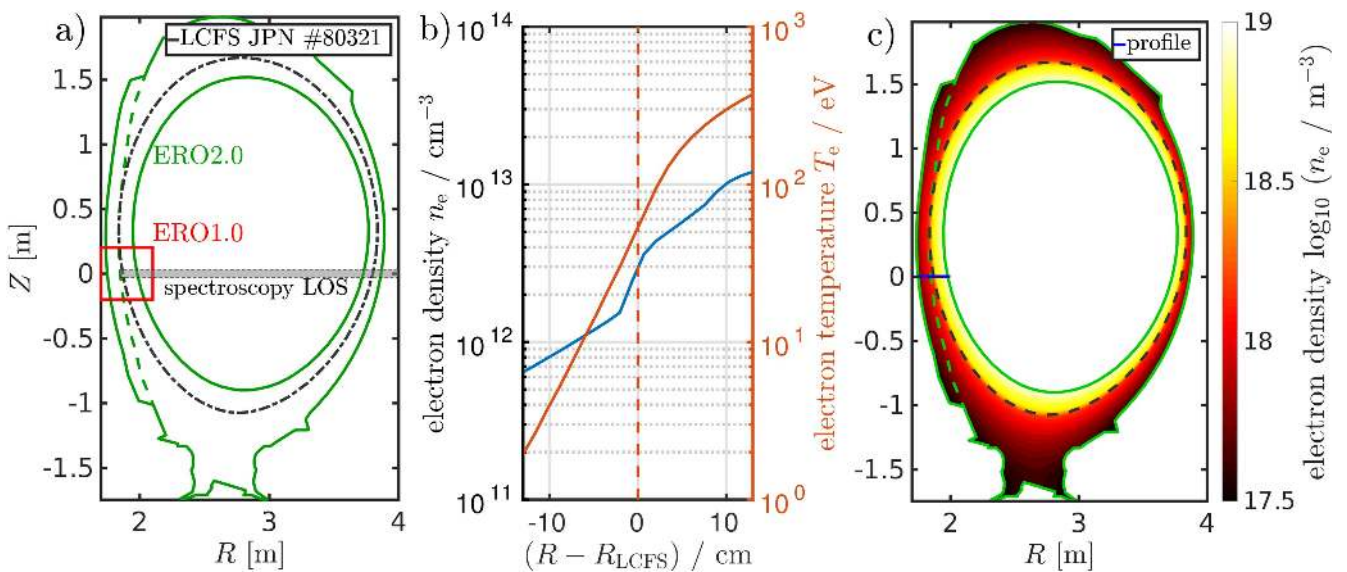


Figure 2. (a) Poloidal view of the density scan experiment described in [9, 17]. The red solid rectangle shows the boundaries of the ERO1.0 simulation volume. The green contours show the boundaries of the new ERO2.0 simulation volume. The dashed lines show the LCFS for JPN #80321 and the ridge of the inner wall guard limiters. (b) Profiles of n_e and T_e at the inner midplane, calculated with the two-point model. (c) Full poloidal (R, z) -map of n_e , calculated with the two-point model and used as the input plasma background in ERO2.0 simulations. The horizontal blue line in (c) indicates the profile location for (b).

e.g. sputtering and re-deposition), using spatial partitioning tree structures such as the octree [15].

- Reduction of memory consumption for large 3D plasma background data by splitting the grid into sub-domains. The data for a sub-domain is dynamically loaded into memory from the input file when a particle enters the sub-domain boundaries.
- Efficient input and output of files using the HDF5 file format [16], which e.g. supports quick reading of data chunks into grid sub-domains.
- Reduction of memory consumption for recording particle probability density in 3D by usage of sparse matrices.

3. Experiments and modeling

The modeling performed within the present study is based on an experiment dedicated to the determination of Be FW

erosion [17]. In this experiment, a series of limiter plasmas with ohmic heating and contact point at the inner wall (IW) was used to experimentally determine Be yields, using LOS integrated passive spectroscopy of Be atoms, Be ions and BeD molecules. The last closed flux surface (LCFS) for the JET pulse number (JPN) #80321 from the above described experiment is shown in figure 2(a) along with the spectroscopy LOS. The gas fuelling rate has been varied ('density scan'), resulting in variation of electron density and electron temperature, which show an inverse relationship. Thus, the dependence of experimental sputtering yields on the electron temperature T_e could be determined. These results were recently used for validating Be sputtering yields and the Be transport model of ERO1.0 [9].

The present work can be seen as a continuation of the modeling efforts presented in [9], but with the simulation volume increased substantially as illustrated in figure 2(a).

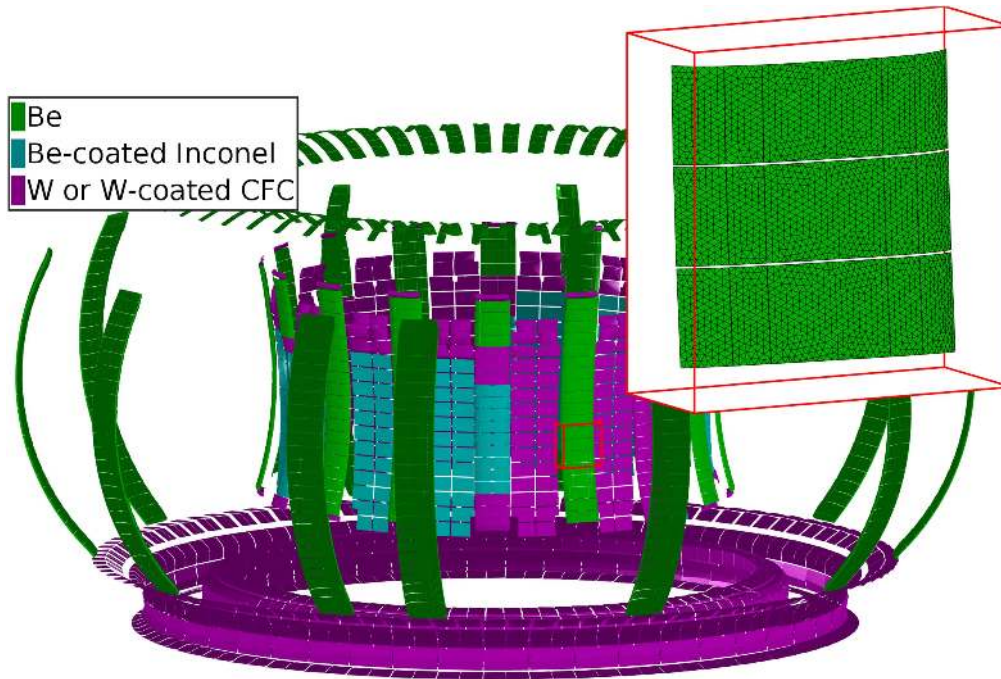


Figure 3. 3D view of the polygon mesh used by ERO2.0, representing selected wall components of the JET ILW. Polygons are color-coded with material composition as indicated in the legend. The inset shows the magnified limiter tiles included in earlier ERO1.0 simulations [9] and also illustrates the typical polygon resolution.

While the ERO1.0 volume was limited to the close surroundings of the spectroscopy observation spot, the ERO2.0 volume covers the entire (in both poloidal and toroidal directions) edge of the plasma. The simulation volume is bounded only in radial direction in-between the wall (outer boundary) and a plasma flux surface that marks the transition to the core plasma (inner boundary) at a specified radius ρ_c . The role of the boundary conditions on Be transport results will be discussed below. We focus on the added information provided by ERO2.0, namely the PWI results for a larger set of PFCs, non-local Be transport, and its verification with experimental wide-angle camera images, which are measuring light emission of impurities in the poloidal cross-section.

3.1. Plasma background

The magnetic field \vec{B} for the present ERO2.0 simulations was obtained from the JET EFIT code [18]. The electron density n_e and temperature T_e , given as 2D maps in the (R, z) -plane, are obtained from [9]. They result from combining radial experimental profiles from reciprocating probe, Thompson scattering, embedded probe and spectroscopic measurements, which are then extrapolated along magnetic field lines to the entire (R, z) -plane using the two-point model as described in [19]. Four such maps are available for shots comparable to JPN #80321. These maps were parametrized with the line-integrated density signal from interferometry and interpolated accordingly to obtain plasma backgrounds for specific shots, e.g. for JPN #80321. Figure 2(b) shows electron density and

temperature profiles interpolated at the inner mid-plane near the LCFS and figure 2(c) the electron density for the full (R, z) -map.

3.2. Wall geometry

The polygon mesh for JET wall components that was used in this work is shown in figure 3 and was provided by the PFCFlux code [20] and post-processed for ERO2.0 requirements, e.g. redundant polygons at the backsides of PFCs were removed. The inset in the red box is a magnification of the three limiter tiles investigated in the earlier ERO1.0 modeling [9], and also shows the edges of the polygons in order to illustrate the typical polygon resolution of ca. 0.7 cm edge length. The polygons can in principle be subdivided in order to increase the resolution, however a sensitivity scan showed that the impact on surface-integrated results (e.g. the total number of eroded atoms) is negligible, so the resolution shown in the figure is sufficient. However, some very fine details such as the castellation of Be tiles [21] or bolt holes [2] are not described by the polygon mesh and are therefore neglected in this work.

The color coding in figure 3 indicates the material composition of the wall elements. The majority of tiles from the inner wall guard limiters (IWGLs), which are the main erosion zones in the limiter shots considered here, are made of bulk Be. In the vicinity of neutral beam injection shinethrough areas, tiles from IWGL center sections are recessed and clad with W-coated carbon-fiber composite (CFC) or Be-coated Inconel [2]. The latter are treated as bulk Be tiles in the current simulations and

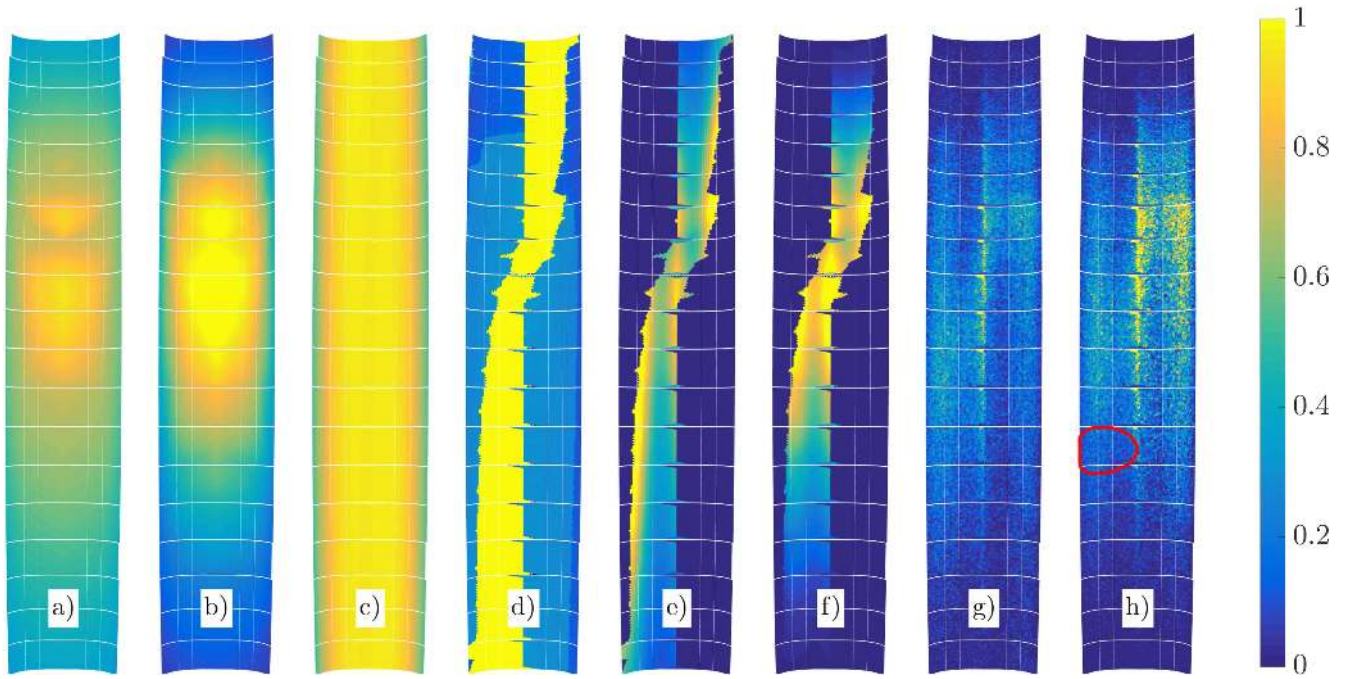


Figure 4. Color-maps (normalized to respective maximum value) of selected surface parameters and PWI results for the IWGL in JET octant 7X. The respective quantities are (a) electron density $n_e/(2 \times 10^{12} \text{ cm}^{-3})$, (b) electron temperature $T_e/(30 \text{ eV})$, (c) magnetic angle (relative to the surface normal) $\theta_B/90^\circ$ (d) connection length $L/(6 \text{ m})$, (e) incident D flux $\Gamma_D^{\text{in}}/(10^{18} \text{ cm}^{-2} \text{ s}^{-1})$, (f) sputtered Be flux $\Gamma_{\text{Be} \leftarrow \text{D}}^{\text{ero}}/(10^{17} \text{ cm}^{-2} \text{ s}^{-1})$, (g) incident Be flux $\Gamma_{\text{Be}}^{\text{in}}/(5 \times 10^{16} \text{ cm}^{-2} \text{ s}^{-1})$, and (h) self-sputtered Be flux $\Gamma_{\text{Be} \leftarrow \text{Be}}^{\text{ero}}/(10^{16} \text{ cm}^{-2} \text{ s}^{-1})$. The red oval in (g) shows the spectroscopic system observation spot used previously for determining effective yields experimentally [17] and by ERO1.0 modeling [9]. The figure illustrates the workflow of the ERO2.0 modeling with chronological ordering from (a) to (h). (a)–(c) result simply from interpolating the input plasma background at the surface cell locations. (d) results from tracing the magnetic field lines. (e)–(f) result from applying (1) and (3), respectively. (g)–(h) result from following the deposition of and self-sputtering (4) by Be test particles eroded by D impact in (f).

are shown in the figure for better visibility of the recessed tiles only. Due to being recessed a few centimeters into the shadowed zone, the coated tiles show negligible erosion, therefore only the bulk Be tiles are of interest in this work.

3.3. Sputtering yields

For the present modeling Be is assumed to be the only relevant impurity in the deuterium (D) plasma. Consequently only two contributions to Be sputtering are considered, namely physical sputtering by D and by Be (self-sputtering). Chemically assisted physical sputtering, which can contribute up to one third of the overall erosion but practically vanishes at high Be limiter temperatures ($T_{\text{surf}} > 520^\circ$) [17], was neglected for the present work. ERO uses the Eckstein formula for the sputtering yield $Y = Y(E_{\text{in}}, \theta_{\text{in}})$ [22] in the case of sputtering by test particles for which E_{in} and θ_{in} are known. The Eckstein fit parameters were obtained from molecular dynamics and binary collision approximation calculations, with the assumption of 50% D content in the Be surface (labeled ‘ERO-min’ due to the yields being 3–4 times lower than for clean Be surfaces), which was recently shown to give good quantitative agreement with JET experiments for plasma-wetted areas [9].

For sputtering by the D^+ ions of the plasma background, pre-calculated effective sputtering yields $Y = Y^{\text{eff}}(T_e, \theta_B)$ are

used, with θ_B being the magnetic inclination angle. These effective yields were obtained by averaging the Eckstein formula, with the angle and energy distributions of incident ions obtained from a semi-analytical approach described in [23].

3.4. Modeled erosion of IWGL wall tiles

Figure 4 shows a selection of surface parameters and PWI results obtained for JPN #80321 at $t = 50 \text{ s}$. Only the IWGL in JET octant 7X is shown, which is a non-recessed limiter with bulk Be tiles. Figures 4(a)–(c) shows the electron density n_e , electron temperature T_e and magnetic angle θ_B at the sheath entrance respectively, which are the plasma background values evaluated at the surface cell centers. Figure 4(d) shows the connection lengths L . These were calculated by tracing magnetic field lines from the centers of each surface cell, until either another surface cell is reached or the connection length exceeds the selected threshold $L_{\text{thr}} = 6 \text{ m}$. The pattern with the inversion at the plasma contact point is characteristic for limiter plasmas and is in good agreement with PFCFlux calculations [20] and heat flux patterns obtained from infra-red (IR) cameras [21]. The shadowing pattern is also visible in the light emission of eroded Be experimentally measured with 2D wide-view cameras (figure 7(b)) as discussed further below. Figure 4(e) shows the

Table 1. PWI results integrated over all IW tiles. n^{in} are rates of incident D and Be particles, n^{ero} are Be sputtering rates by D and Be impact respectively, and $Y_{\text{eff}}^{\text{tot}}$ are the corresponding effective yields.

	D	Be
n^{in} (s ⁻¹)	7.7×10^{22}	3.3×10^{20}
n^{ero} (s ⁻¹)	6.8×10^{20}	8.2×10^{19}
$Y_{\text{eff}}^{\text{tot}}$	9×10^{-3}	0.25

D ion flux

$$\Gamma_{\text{D}}^{\text{in}} = n_{\text{e}} \cdot c_{\text{s}} \cdot \cos(\theta_{\text{B}}) \cdot S \quad (1)$$

reaching the surface, with the ion sound velocity

$$c_{\text{s}} = \sqrt{k_{\text{B}}(T_{\text{e}} + T_{\text{i}})/m_{\text{i}}}, \quad (2)$$

the magnetic inclination angle θ_{B} and shadowing factor S . The latter is introduced as a correction factor between 0 and 1, which accounts for the fact that fewer ions should reach magnetically shadowed zones. A simple shadowing model with $S = 0$ for cells with $L < L_{\text{thr}}$ (shadowed) and $S = 1$ for cells with $L = L_{\text{thr}}$ (plasma-wetted) is used. Figure 4(f) shows the eroded Be ion flux

$$\Gamma_{\text{Be} \leftarrow \text{D}}^{\text{ero}} = \Gamma_{\text{D}}^{\text{in}} Y_{\text{Be} \leftarrow \text{D}}^{\text{eff}}(T_{\text{e}}, \theta_{\text{B}}). \quad (3)$$

Figure 4(g) shows the Be ion flux $\Gamma_{\text{Be}}^{\text{in}}$ reaching the surface resulting from following the test particles until they impact on the wall. Noteworthy, the simulated Be incidence ion flux does not show the sharp distinction between shadowed and plasma-wetted zone which was assumed for the D incidence ion flux in figures 4(e)–(f). This means that self-sputtering can lead to erosion in shadowed regions. However as discussed below, self-sputtering poses a minor contribution to total erosion (compared to sputtering by D ions) for the plasma conditions considered here. Therefore, hardly any Be emission from shadowed zones is observed in the experimental 2D images (see below in figure 7(b)). Figure 4(h) shows the self-sputtered Be ion flux

$$\Gamma_{\text{Be} \leftarrow \text{Be}}^{\text{ero}} = \Gamma_{\text{Be}}^{\text{in}} Y_{\text{Be} \leftarrow \text{Be}}(E_{\text{in}}, \theta_{\text{in}}) \quad (4)$$

which is calculated by adding up the contribution of all impacting test particles to the self-sputtering. Be erosion by self-sputtering $\Gamma_{\text{Be} \leftarrow \text{Be}}^{\text{ero}}$ is lower than D sputtering $\Gamma_{\text{Be} \leftarrow \text{D}}^{\text{ero}}$, which can be attributed to the incidence Be flux being much lower than the D flux.

This can be further quantified by calculating the total number of incidence or eroded atoms per second $n = \sum_i \Gamma_i \cdot a_i$ across all IW surface cells with area a_i . As a rough measure for effective yields, we can define $Y_{\text{eff}}^{\text{tot}} = n^{\text{ero}}/n^{\text{in}}$. Table 1 shows the results. While the effective yield is ~ 28 times higher for Be self-sputtering, the Be incidence rate is ~ 235 times lower than the D incidence rate, therefore $n_{\text{Be} \leftarrow \text{Be}}^{\text{ero}}$ is a factor ~ 8 lower than $n_{\text{Be} \leftarrow \text{D}}^{\text{ero}}$. It should be noted that these results are dependent on plasma backgrounds taken by ERO as an input.

3.5. Modeled Be transport

For understanding the composition of the above $Y_{\text{eff, Be} \rightarrow \text{Be}}$ value, we need to take into account Be transport results. For the transport calculations, an ensemble of 2×10^6 eroded Be test particles was launched⁹. In addition to the Lorentz force and friction with the background plasma ions (described by a Fokker–Planck collision term [24]), test particles are affected by anomalous cross-field transport. It is treated in ERO as a diffusion process with a constant coefficient D_{\perp} as an open parameter. In the simulations shown here, $D_{\perp} = 1 \text{ m}^2 \text{ s}^{-1}$ was assumed for Be ions in the entire plasma edge, which is in the order of the Bohm diffusion coefficient $D_{\perp}^{\text{Bohm}} = (k_{\text{B}} T_{\text{e}})/(16eB)$ [25] for $B \approx 4.2 \text{ T}$ and $T_{\text{e}} \approx 55 \text{ eV}$ at the LCFS in figure 2(b). A sensitivity scan for the impact of D_{\perp} on ERO1.0 results can be found in [26].

A major particle fraction of 65% reaches the surface as Be^{2+} , followed by 16% Be^{3+} , 13% Be^{+} , 5% Be^{4+} and $< 1\%$ Be^0 . Figure 5 shows the distributions for impact energy and angle, accumulated over all PFC tiles.

The angular distributions (figure 5(a)) for each charge state show a characteristic shape with a monotonic increase from $\theta_{\text{in}} = 0^\circ$ (normal incidence) to about $\theta_{\text{in}} \approx 50^\circ$, followed by a peak which is more pronounced for low charge states Z . With increasing Z , the peak position gets shifted to higher θ_{in} (shallow incidence). The total distribution has a mean at $\theta_{\text{in}} = 54^\circ$. For shallow magnetic field angles relevant for the JET-ILW limiters or ITER blanket modules, similar values are found in literature with ERO1.0 calculations [9] for D ions, and analytic [27] and particle-in-cell calculations [28] for D and carbon (C) ions.

Because incoming charged particles obtain a large part $E_{\text{in}} = V_{\text{sheath}} \cdot Z \cdot e$ of their energy in the sheath, the energy distribution (figure 5(b)) is determined by the distribution of charge state Z , and by the local sheath potential V_{sheath} which is proportional to the electron temperature. ERO2.0 assumes $V_{\text{sheath}} = 3k_{\text{B}}T_{\text{e}}/e$ for the sheath potential. With the maximum $T_{\text{e}} = 30 \text{ eV}$ from figure 4(b), the maximum potential is $V_{\text{sheath}} = 90 \text{ V}$. Therefore, each of the energy distributions for an individual charge state Z has a distinctive kink at $E_{\text{in}} = Z \cdot 90 \text{ eV}$. Each kink is followed by a high-energy tail due to the initial thermal energy the particles have before entering the sheath. This tail becomes broader with increasing Z , because higher charged particles have typically travelled longer distances before entering the sheath and are already considerably thermalized with the background plasma. The total energy distribution has a mean at $E_{\text{in}} = 145 \text{ eV}$.

Figure 6 shows the simulated Be density for charge states $Z = 1, 2$ and 3 averaged in toroidal direction and time. For Be^0 (not shown) and Be^{+} , we observe that the penetration depth (determined by the ionization probability) is in the order of several cm, while recombination from higher ionized Be is negligible. Hence, their density is well localized at the erosion sites on the IW. This shows that Be I and II line emission measurements in the observation spot are determined mostly by the Be eroded within the same observation

⁹ The calculation has required $T \approx 17\text{h}$ on 192 JURECA CPU cores.

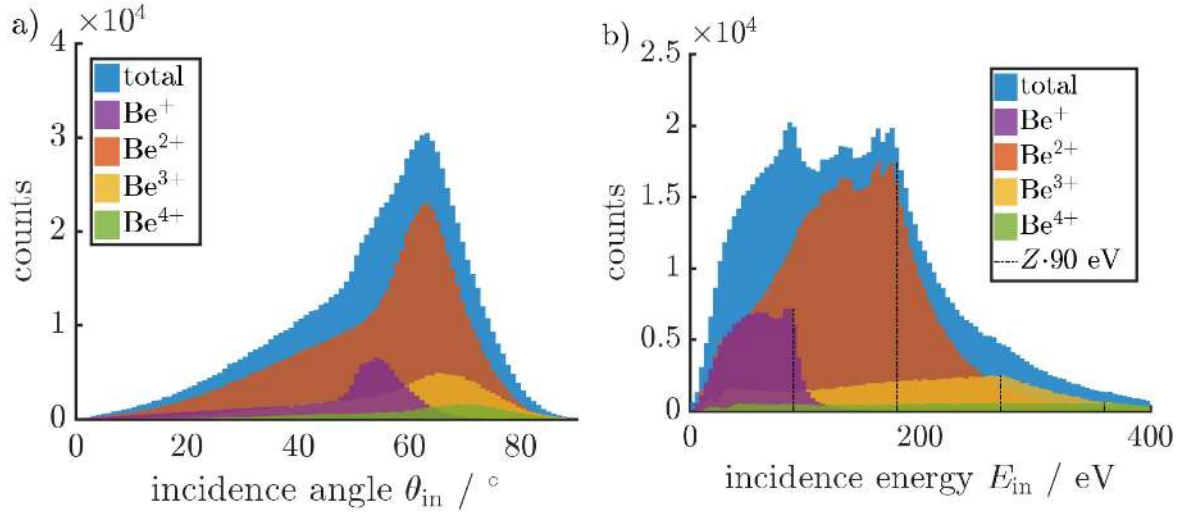


Figure 5. Distributions of Be incidence (a) angle (relative to the surface normal) and (b) energy, accumulated over all PFC tiles. The total counts are shown, and also the contributions from individual charge states. For the energy distributions, vertical lines mark the locations of kinks at $E_{in} = Z \cdot 90$ eV which are due to the maximum sheath potential drop at the limiter surface.

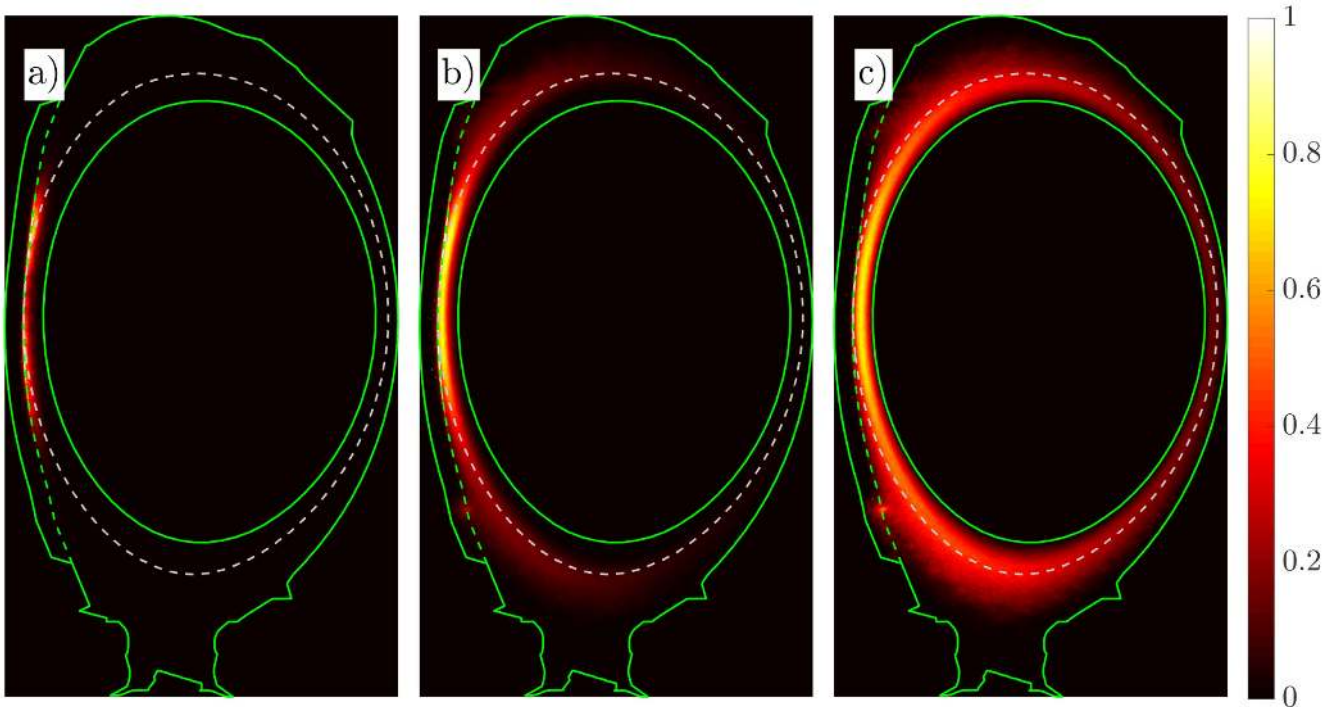


Figure 6. Color-maps (normalized to the respective maximum value) showing calculated Be density in the (R, z) -plane averaged over toroidal angle and time. (a) $n_{Be^+}/(4 \times 10^{16} \text{ m}^{-3})$, (b) $n_{Be^{2+}}/(2 \times 10^{17} \text{ m}^{-3})$, (c) $n_{Be^{3+}}/(1 \times 10^{17} \text{ m}^{-3})$. The solid green lines show the simulation volume boundaries, the dashed white line shows the separatrix for the density scan shot JPN #80321 at $t = 50$ s.

spot or up to a few cm away. This supports previous determination of LOS-averaged effective yields [9, 17], which assumed Be line emission to be originated from particles eroded directly within the observation spot.

From figure 6 we see that Be with $Z > 2$ penetrates much deeper into the plasma. These particles can in principle reach locations at larger distance from the erosion source after completing one or more poloidal turns and contribute to self-sputtering. However the distributions in figure 5 show only a minor fraction (about 20%) of particles with $Z > 2$. This

discrepancy can be attributed to the fraction of test particles crossing the ERO2.0 simulation volume boundaries, which are shown as green solid lines in figures 2(a) and 6. While 49% of the test particles deposit on the surface of the 3D limiter geometry (and contribute to the distributions in figure 5 and to self-sputtering), the remaining 51% leave the simulation volume at the boundaries (39% at the inner and 13% at the outer boundary).

The outer boundary corresponds to the (R, z) -projection of the JET FW, which was retracted on the left side in order to

contain the three-dimensional IWGL surface. The 13% of particles absorbed at this boundary are travelling into gaps between limiter tiles or onto other PFCs which were not included in the set of 3D polygon meshes (e.g. the Be parallel protection bars below the IWGLs) and are of no further interest in this work. However, the 39% of particles entering the core plasma (which are currently assumed as lost in the simulation) may influence the outcome significantly in reality. After being confined in the core plasma for a certain time, particles should re-enter the SOL due to anomalous cross-field transport (see equation (6.2) in [25]).

This fraction of particles can in principle be accounted for in ERO2.0 by setting the specified simulation volume boundary ρ_c to smaller values or even dropping the inner boundary entirely, allowing test particles to freely enter and leave the core plasma. The disadvantage is that calculation time increases dramatically by a factor of 10 or more due to the much longer trajectory lengths of the core impurities (because ERO calculates trajectories in full orbit resolution in 3D, small time steps of the order of nanoseconds are required to prevent numerical errors). More importantly, ERO is not developed for core transport simulations, for instance radial dependence of the anomalous diffusion coefficient D_{\perp} is not considered in the code. In order to account for the particles re-entering the SOL from the core, an alternative boundary condition is currently being investigated. In this boundary condition, particles entering the core region are re-emitted into the SOL at a random location on the separatrix.

3.6. Synthetic wide-angle 2D camera images

For validating the erosion patterns shown in figure 4 and Be^+ density patterns shown in figure 6, comparison to experimental images from wide-angle 2D cameras can be used. For this purpose, a new synthetic diagnostics that mimics experimental images has been implemented into ERO2.0. For rendering images, ERO2.0 can choose between a ray tracing algorithm and a perspective projection matrix algorithm. Both algorithms utilize a simple optical model in which the camera is approximated as a pinhole camera with a certain pupil position and LOS direction, however the implementation of the algorithms is different. The ray tracing is more computationally efficient for rendering the wall, while the perspective matrix is more efficient for rendering impurity line emission because ERO2.0 stores 3D emission densities as sparse matrices.

Figure 7(a) shows the field of view of an experimental camera. The grayscale image was taken from a shot with a disruption flash in which the JET wall is well visible. By fitting selected image points with corresponding points on the JET 3D wall geometry model using the Python package CALCAM¹⁰, the camera parameters such as the pupil position and LOS could be obtained. Figure 7(a) illustrates the alignment of experimental images with the synthetic ones. One can see that there is misalignment in some image regions (mostly on the image borders where optical aberrations are

the strongest), however the relevant image regions where Be emission occurs are well aligned.

As no Be emission images were available from the density scan experiment, instead we use images measured parasitically in limiter discharges (reference shot JPN #91140) with the plasma shifted upward compared to JPN #80321. To obtain a plasma parameters (R, z)-map as in figure 2(c), a translation and ‘squeezing’ transformation was applied. Figure 7(b) shows an overlay of the wireframe with the experimental image of Be II 467 nm line intensity (colored) from JPN #91140. Figure 7(c) shows a similar overlay for the intensity simulated by ERO2.0. One can see that ERO2.0 can qualitatively well reproduce the emission patterns from the experiment. Because Be^+ is localized at the erosion areas, the image reflects the erosion patterns from figure 4, with the above-described shadowing pattern as the most striking feature. We observe two distinct emission ‘plumes’ from the IWGLs in octants 4Z (left side of image) and 5Z (center of image). The emission plume of the IWGL in-between in octant 5X is limited to the five tiles at the top, because the other tiles are recessed and therefore not eroded.

Some subtle differences between experiment and modeling are yet visible, which are marked as regions I–III in the figure. In region I, the emission plumes at the IWGLs in the experimental image extend more in z -direction up to the top IWGL tiles compared to the synthetic image. This might indicate that the T_e in the ERO2.0 plasma background has a too short SOL decay length, so that the upper tiles do not get eroded in the model. In region II, the plume in octant 5Z has a different shape: it is thinner near the plasma contact point and becomes broader near the limiter ends in the experiment, while in the modeling the plume has approximately equal thickness everywhere which is also seen in the Be^+ density in figure 6(a). This again might be due to uncertainties in the plasma background used for modeling. The plume width is determined mostly by the ionization rate for Be^0 or Be^+ , which in turn is given by the product of the corresponding ionization rate coefficient (obtained from the ADAS code database [29]) and n_e . While the rate coefficient shows only a slight dependence on n_e and T_e in the parameter range of interest, an underestimation of the electron density n_e in the plasma background may well account for the too broad emission plume. A more thorough benchmarking would require comparison to Be I experimental images which were not available at the time of writing this manuscript. Finally in region III, an emission plume is visible in the experimental image below the IWGL in octant 5Z, which is missing from the synthetic image. This can be attributed to erosion of the Be parallel protection bars [2], which are currently missing in the ERO2.0 ILW geometry.

Apart from the plasma background, the diffusion coefficient $D_{\perp} = 1 \text{ m}^2 \text{ s}^{-1}$ was also expected to be a source of uncertainty and affect e.g. the plume width in region II. Therefore the simulations were repeated with two different coefficients $D_{\perp} = 0.1 \text{ m}^2 \text{ s}^{-1}$ and $D_{\perp} = 10 \text{ m}^2 \text{ s}^{-1}$. However, the images resulting from the sensitivity scan (not shown) have only a very weak dependence on D_{\perp} . In toroidal direction, the emission plumes are slightly more stretched for low

¹⁰ <https://github.com/euratom-software/calcam>

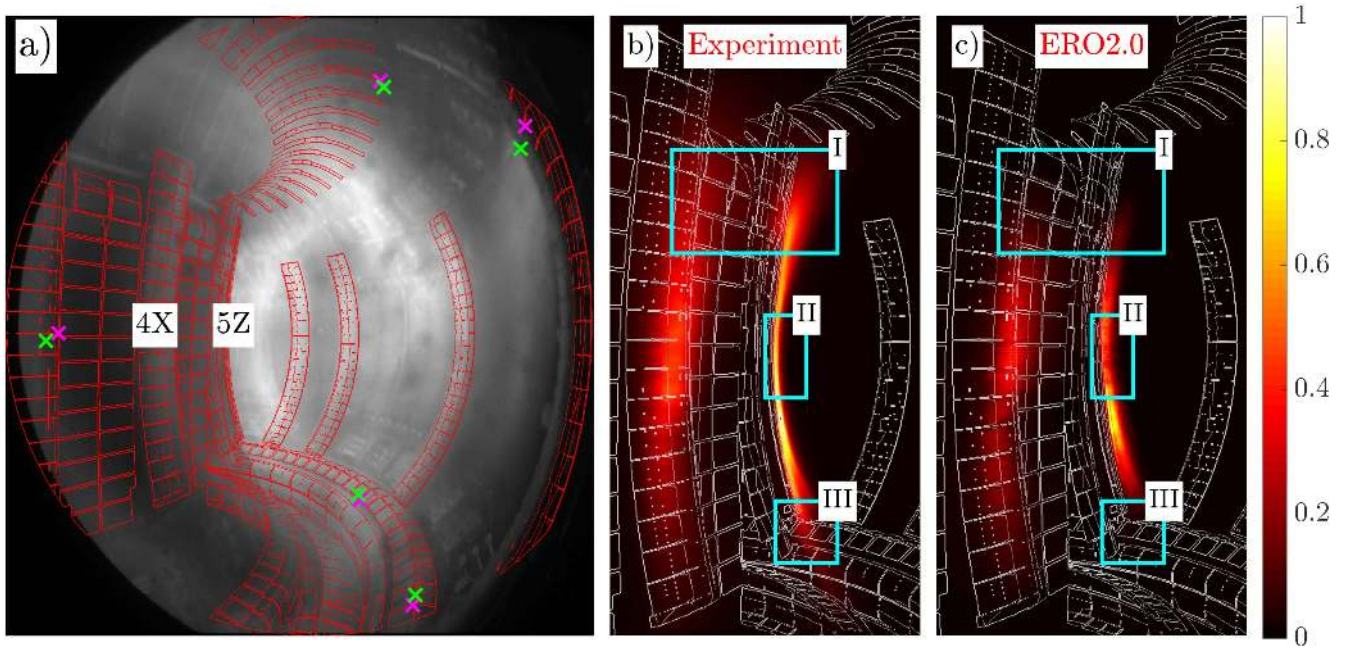


Figure 7. Comparison of experimental 2D images from a JET wide-angle camera (KL1-E4WC, Be II 467 nm filter) and the corresponding synthetic images calculated by ERO2.0. (a) Overlay of an experimental image (grayscale) of a disruption, during which the wall is fairly visible, with a wireframe model of the wall (red) rendered by ERO2.0. Four reference point pairs (green: experiment, magenta: synthetic) are shown in order to illustrate regions where the two images are misaligned. The misalignment occurs mostly at the image borders where optical aberrations are the strongest. Also there is a misalignment in the divertor region of the image that is closer to the image center. This suggests a certain inaccuracy in the line-of-sight and pupil position of the synthetic camera model. However, the misalignment in the relevant image parts, where the most Be line emission occurs (IW, octants 4X and 5Z), is small enough that it does not affect the general picture and the discussed comparison of synthetic and experimental emission. (b) Overlay of the same wireframe model (white) with an experimental image from JPN #91140 of the same camera showing the Be II emission intensity. (c) The same, with the Be II emission rendered by the ERO2.0 synthetic camera model from the simulated volumetric emission data. The color scaling has arbitrary units.

values and more compressed for high values of D_{\perp} , because cross-field transport obstructs the transport along field lines, but the poloidal and radial shape of the plumes are not affected.

4. Discussion and conclusions

The new code version ERO2.0 has been developed, which contains several principal technical innovations. Among these are a more flexible definition of the wall geometry and a parallelization scheme, which allows to simulate several hundred more particles with only marginal increase in computing time. These innovations allow a significant increase of the simulation volume. In order to demonstrate the resulting new modeling capabilities, simulations for JET limiter plasmas were performed.

Erosion patterns due to D and Be impact were calculated. The erosion rate due to D impact was shown to be eight times higher than Be self-sputtering. The distributions of incident Be were discussed, with the mean incidence angle being 54° and most Be reaching the surface with $Z = 2$. However, the calculations did not take into account Be particles re-entering the SOL from the core plasma. The modeled self-sputtering is therefore currently underestimated, which is expected to improve after implementing a boundary condition which restores the particle balance.

A novel synthetic diagnostic has been developed, which uses the calculated 3D impurity density to render synthetic 2D wide-angle camera images. These show a good qualitative agreement with the respective experimental images for Be II line emission, which increases confidence in the PWI and impurity transport model.

The remaining deviations from experiment in the 2D camera images are attributed to uncertainties in n_e and T_e in the input plasma backgrounds calculated by the basic two-point model. In particular, the extrapolation of plasma parameters along field lines behind the IW limiter ridge is problematic and seems to give too low values for the top and bottom of the limiters, which results in an underestimation of the Be erosion and light emission in these areas.

Apart from these uncertainties, the ion temperature, electric potential and ion flow velocity are based on estimations as diagnostic data is not available. We assumed equipartition $T_i = T_e$ in the plasma edge. The ion temperature T_i affects simulation results via the ion sound velocity (2), which in turn affects the estimated ion flux (1) and thereby the erosion fluxes. However, the calculation of other important quantities such as sputtering yields, transport (e.g. by ionization and recombination rates), photon emissivity coefficients etc. are parametrized in T_e and are therefore not affected. The electric potential was set to zero, except for the Debye and magnetic pre-sheath, where it was calculated using equations (1) and (2) in [23]. The parallel and radial electric fields

occurring in the SOL [12], which are much smaller than those in the sheath, were neglected in this work. The background ion flow velocity, which is directed towards the closest PFC along a field line in the SOL, was previously shown to play an important role in non-local Be transport [19]. Therefore, the 3D ion flow field in the SOL was calculated here using the ‘simple SOL’ model (equation (3.9c) in [30]). Outside the SOL it was assumed to be zero.

To improve the ERO2.0 simulations, dedicated modeling of JET limiter plasma backgrounds using the edge code SOLEDGE2D [31] is currently ongoing. The new plasma background are expected to provide more accurate values of n_e and T_e as well as information about ion temperature, flow velocity and electric fields. Benchmarking with further experimental diagnostics, such as Z_{eff} measurements, wide-view 2D camera images and LOS-integrated signals for various Be I and Be II emission lines, and IR cameras, should be performed in order to reduce model uncertainties and further increase confidence in predictive modeling for ITER.

Acknowledgments

This work has been carried out within the framework of the EUROfusion Consortium and has received funding from the Euratom research and training programme 2014–2018 under grant agreement No 633053. The views and opinions expressed herein do not necessarily reflect those of the European Commission. The authors gratefully acknowledge the computing time granted by the JARA-HPC Vergabegremium on the supercomputer JURECA at Forschungszentrum Jülich.

ORCID iDs

J Romazanov  <https://orcid.org/0000-0001-9439-786X>

D Borodin  <https://orcid.org/0000-0001-8354-1387>

A Kirschner  <https://orcid.org/0000-0002-3213-3225>

S Brezinsek  <https://orcid.org/0000-0002-7213-3326>

M Firdaouss  <https://orcid.org/0000-0002-6921-0116>

P Gibbon  <https://orcid.org/0000-0002-5540-9626>

A Lasa  <https://orcid.org/0000-0002-6435-1884>

Ch Linsmeier  <https://orcid.org/0000-0003-0404-7191>

References

- [1] Pitts R A et al 2011 *J. Nucl. Mater.* **415** S957–64
- [2] Matthews G F et al 2011 *Phys. Scr.* **T145** 014001
- [3] Brezinsek S 2015 *J. Nucl. Mater.* **463** 11–21
- [4] Naujoks D et al 1993 *Nucl. Fusion* **33** 581–90
- [5] Borodin D et al 2011 *Phys. Scr.* **T145** 014008
- [6] Kirschner A et al 2016 *Contrib. Plasma Phys.* **56** 622–7
- [7] Ding R et al 2017 *Nucl. Fusion* **57** 056016
- [8] Ding R et al 2017 *Nucl. Mater. Energy* (in press) (<https://doi.org/10.1016/j.nme.2017.03.012>)
- [9] Borodin D et al 2014 *Phys. Scr.* **T159** 014057
- [10] Abrams T et al 2017 *Nucl. Fusion* **57** 056034
- [11] Kirschner A et al 2015 *J. Nucl. Mater.* **463** 116–22
- [12] Kirschner A, Philipps V and Winter J 2000 *Nucl. Fusion* **40** 989
- [13] Jülich Supercomputing Centre 2016 *JLSRF* **2** A62
- [14] McCool M D, Reinders J and Robison A 2012 *Structured Parallel Programming: Patterns for Efficient Computation* (San Francisco, CA: Morgan Kaufmann)
- [15] Salomon D 2011 *The Computer Graphics Manual Vol 2* (London: Springer)
- [16] Folk M et al 2011 *Proc. EDBT/ICDT 2011 Workshop on Array Databases* pp 36–47 (<https://doi.org/10.1145/1966895.1966900>)
- [17] Brezinsek S et al 2014 *Nucl. Fusion* **54** 103001
- [18] Brix M et al 2008 *Rev. Sci. Instrum.* **79** 10F325
- [19] Miettunen J et al 2013 *J. Nucl. Mater.* **438** S612–5
- [20] Firdaouss M et al 2013 *J. Nucl. Mater.* **438** S536–9
- [21] Arnoux G et al 2013 *Nucl. Fusion* **53** 073016
- [22] Eckstein W 2008 *Vacuum* **82** 930–4
- [23] Borodkina I et al 2016 *Contrib. Plasma Phys.* **56** 640–5
- [24] Montgomery D C and Tidman D A 1964 *Plasma kinetic theory* (New York: McGraw-Hill)
- [25] Stangeby P C 2000 *The Plasma Boundary of Magnetic Fusion Devices* (Bristol: IOP Publishing)
- [26] Lasa A et al 2017 *Nucl. Fusion* (submitted)
- [27] Schmid K et al 2010 *Nucl. Fusion* **50** 105004
- [28] Kawamura G, Tomita Y and Kirschner A 2013 *J. Nucl. Mater.* **438** S909–12
- [29] Summers H P and O’Mullane M G 2005 *The atomic data and analysis structure Nuclear Fusion Research: Understanding Plasma-Surface Interactions* ed R E H Clark and D H Reiter (Berlin: Springer) pp 399–413
- [30] Stangeby P and McCracken G 1990 *Nucl. Fusion* **30** 1225–379
- [31] Bufferand H et al 2013 *J. Nucl. Mater.* **438** S445–8